optica

Terahertz difference-frequency quantum cascade laser sources on silicon

Seungyong Jung,[1,3] Jae Hyun Kim,[1] Yifan Jiang,[1] Karun Vijayraghavan,[2] and Mikhail A. Belkin[1,4]

[1]Department of Electrical and Computer Engineering, The University of Texas at Austin, 10100 Burnet Road, Austin, Texas 78758, USA
[2]ATX Photonics, 10100 Burnet Road, Austin, Texas 78758, USA
[3]e-mail: sejung@utexas.edu
[4]e-mail: mbelkin@ece.utexas.edu

Received 10 October 2016; revised 24 November 2016; accepted 30 November 2016 (Doc. ID 278379); published 22 December 2016

Terahertz quantum cascade laser sources based on intra-cavity frequency mixing are currently the only monolithic electrically pumped semiconductor devices that can operate in the 1–6 THz spectral range at room temperature. The introduction of the Cherenkov waveguide scheme in these devices grown on semi-insulating InP substrates enabled generation of tens of microwatts of average terahertz power output and wide spectral tunability. However, terahertz radiation outcoupling in these sources is still highly inefficient. Here we demonstrate that an application of the III–V-on-silicon hybrid laser concept to terahertz quantum cascade laser sources based on Cherenkov intra-cavity difference-frequency generation dramatically improves their output power and mid-infrared-to-terahertz conversion efficiency. The best-performing device transfer-printed on a float-zone high-resistivity silicon substrate produced 270 μW of peak power output at 3.5 THz at room temperature, a factor of 5 improvement over the best reference devices on a native semi-insulating InP substrate.

OCIS codes: (130.3120) Integrated optics devices; (140.5965) Semiconductor lasers, quantum cascade; (190.5970) Semiconductor nonlinear optics including MQW.

https://doi.org/10.1364/OPTICA.4.000038

1. INTRODUCTION

The terahertz (THz) spectral region, spanning from 0.3 to 10 THz, hosts numerous applications including chemical and biomedical sensing, non-invasive imaging and security screening, radio astronomy, and spectroscopy [1,2]. Highly desired for THz systems are compact, mass-producible sources with room temperature operation, electrical pumping, high power, and wide tunability. THz quantum cascade lasers (QCLs) are the only electrically pumped semiconductor lasers that can operate in the 1–5 THz spectral range without strong magnetic fields [3]. THz QCLs can now produce up to watt-level peak power output in pulsed mode [4] and tens of milliwatts of optical power in continuous wave (CW) operation. However, the operation of THz QCLs is still limited to cryogenic temperatures [5,6].

To produce THz QCL sources operable at room temperature, a technology based on intra-cavity difference-frequency generation (DFG) in mid-infrared (mid-IR) QCLs has been proposed and developed [7]. These THz DFG-QCL devices have active regions designed to provide both gain for mid-IR pump waves and giant second-order nonlinearity ($\chi^{(2)}$) for THz DFG inside of the laser cavity [8]. Since THz DFG does not require population inversion across the THz transition, THz DFG-QCLs can provide coherent THz emission at room temperature [9]. THz output power and tunability of THz DFG-QCLs have been remarkably improved in recent years after the implementation of the Cherenkov emission scheme [10].

Cherenkov THz DFG-QCLs reported so far use a semi-insulating (SI) InP substrate. SI InP possesses higher THz refractive index than the refractive index associated with the THz nonlinear polarization wave in the active region. As a result, THz radiation generated in the active region is emitted into the SI InP substrate at the Cherenkov angle of about 20–30 deg [10]. The SI InP substrate has substantially lower THz loss, compared to the QCL active region and allows for relatively efficient extraction of THz radiation from different sections of the laser waveguide. Cherenkov THz DFG-QCLs on SI InP demonstrated broadly tunable THz emission in the 1–6 THz range [11–15], up to 2 mW of THz peak power output in pulsed mode [16], and over 10 μW of THz power output in CW operation [17] at room temperature. However, simulations show that, for a typical 3-mm-long THz DFG-QCL on the SI InP substrates, over 80% of THz light is trapped and absorbed in the substrate due to significant residual THz absorption (see Fig. 1), and the relatively high refractive index in SI InP prevents efficient outcoupling of the THz radiation cone from the front facet.

Here we demonstrate that an application of the III–V-on-silicon (III/V-on-Si) hybrid semiconductor laser concept [18–20] to Cherenkov THz DFG-QCLs can dramatically improve THz extraction efficiency in these devices. Experimentally, the best-performing 4.2-mm-long Cherenkov THz DFG-QCLs transfer-printed [21,22] on float-zone high-resistivity (FZ HR) Si produced

THz peak power output of up to 270 μW with mid-IR-to-THz conversion efficiency of 480 $\mu W/W^2$ at 3.5 THz at room temperature. The THz peak power was 5 times higher and the mid-IR-to-THz conversion efficiency was 8 times higher than those of the best reference devices with the same dimensions on the SI InP substrate.

2. DESIGN

Cherenkov emission occurs in THz DFG-QCLs when the propagation vector of the THz radiation in the device substrate ($\omega_{THz} n_s/c$, where n_s is the refractive index of the substrate) is larger than the propagation vector of the nonlinear polarization wave in the laser active region ($k_{DFG} = \omega_{THz} n_g/c$, where n_g is the group index of the mid-IR pumps [10]). Assuming the waveguide width of a THz DFG-QCL is comparable to or smaller than the THz wavelength, Cherenkov THz emission into the substrate is a cone with an angle θ_c, to the waveguide direction, defined as $\theta_c = \cos^{-1}(n_g/n_s)$; see Fig. 2(a). Since the mid-IR group index in QCLs shows a nearly consistent value of ~3.37 over the 8–12 μm [23], any substrate with a THz refractive index higher than ~3.37 can fulfill the condition of Cherenkov DFG emission.

The SI InP substrate is typically used for THz DFG-QCLs because high-performance mid-IR QCLs with InGaAs/AlInAs active regions can be grown on InP. However, the optical properties of SI InP, shown in Fig. 1, are not perfectly suited for Cherenkov THz DFG. In particular, SI InP has relatively high THz absorption, which prevents efficient THz extraction from the laser waveguides longer than 1–2 mm. Additionally, SI InP has the relatively high THz refractive index, which results in a Cherenkov cone angle of ~20 deg, meaning that substrate facet polishing is needed to avoid total internal reflection of the Cherenkov wave and allow for THz outcoupling to free space [10]. The substrates are polished as a wedge at 20–30 deg. This, however, enables outcoupling of only a portion of the radiation in the center of the Cherenkov cone. Conical substrate polishing may improve THz outcoupling efficiency, but it is difficult to fabricate in practice.

FZ HR Si as a THz DFG-QCL substrate provides many advantages over the SI InP substrate. The refractive index and optical loss of FZ HR Si are given in Fig. 1. The THz refractive index of Si ($n_{Si} \approx 3.42$) is well matched to n_g and is nearly constant in the 1–4.5 THz range and beyond. The THz Cherenkov cone angle in FZ HR Si is approximately 10° across the entire THz range. As a result, THz outcoupling through the flat-polished substrate facet is more efficient in the THz DFG-QCLs on Si. Moreover, the outcoupling of the THz Cherenkov wave in the devices on Si can be realized without facet polishing since the Cherenkov angle in Si is smaller than the critical angle at the Si–air interface. FZ HR Si also has extremely low THz absorption, which allows for efficient extraction of THz radiation in THz DFG-QCLs with long (5–10-mm-long) waveguides.

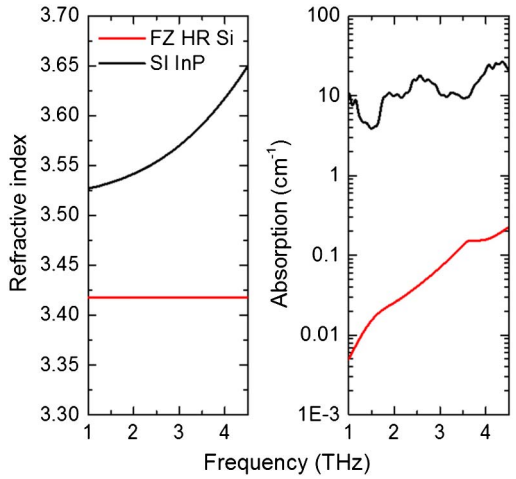

Fig. 1. Refractive indices and absorption coefficients of SI InP and FZ HR Si in the THz range.

Figures 2(c) and 2(d) show the results of a three-dimensional COMSOL simulation of a 203-μm-long section of a Cherenkov THz DFG-QCL operating at 3.5 THz on a SI InP substrate [Fig. 2(c)] and a FZ HR Si substrate [Fig. 2(d)]. The nonlinear-polarization sources in the active region are modeled by dipoles radiating forward-propagating waves at a fixed frequency and oscillating across the layers (TM mode). Simulation results clearly show the different THz Cherenkov cone angles for the devices on Si versus InP, as predicted earlier. The outcoupling efficiency of the THz radiation through the uncoated flat-polished device facet is about 30% and 45% for the devices on the InP and Si substrates, respectively (we assumed 20 deg polishing for InP substrates and 10 deg polishing for Si substrates).

Figure 2(d) displays THz power of a 3.5 THz DFG-QCL on SI InP versus that on FZ HR Si for different cavity lengths. The expected power output from longer devices (P_{THz}) is obtained by scaling the COMSOL simulation results for 203-μm-long devices shown in Figs. 2(c) and 2(d) as

$$P_{THz} = \eta_{ext} I_0 \int_0^{L_{cav}} e^{-\alpha_{sub} x \cos\theta_c} dx, \quad (1)$$

where η_{ext} and I_0 are, respectively, the outcoupling efficiency of the Cherenkov cone through the facet and the linear power density (W/m) of the THz Cherenkov wave emitted from the laser

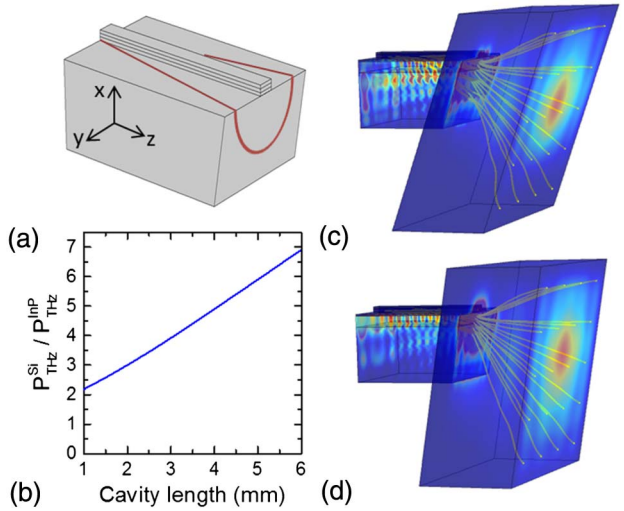

Fig. 2. Cherenkov THz DFG emission in QCLs. (a) The schematic of the Cherenkov emission in a DFG-THz QCL. (b) The ratio of THz power of the Si-hybrid device to THz power of the InP reference device at different cavity lengths. (c), (d) Three-dimensional COMSOL simulation of the THz power intensity outcoupled from the (c) SI InP device to air and the (d) FZ HR Si device to air. The yellow lines are the power streamlines indicating the propagation direction of THz power outcoupled to equal points on the air monitor. All simulations assume uniform mid-IR pumps intensity in the laser cavity.

waveguide into the substrate as determined from the COMSOL simulations. Also, L_{cav} is the laser cavity length, and α_{sub} is the absorption coefficient of the substrate.

The power output of the SI InP device virtually stops increasing after the length of the laser cavity exceeds the absorption length of the THz radiation in the SI InP substrate (<1 mm in 3–5 THz range; see Fig. 1). In contrast, the power output of the hybrid device continuously increases with the cavity length, owing to the extremely long THz absorption length (>5 cm) in FZ HR Si.

3. FABRICATION

To verify these predictions experimentally, the THz DFG-QCL structure was grown on a 660-μm-thick semi-insulating InP substrate by a commercial foundry (IQE Inc.). The active region of our DFG-QCL is designed based on the bound-to-continuum transition scheme [24], and its waveguide structure is similar to that of the device reported in Ref. [11]. The growth started with a 200-nm-thick $In_{0.53}Ga_{0.47}As$ (Si: 1×10^{18} cm^{-3}) current injection/etch-stop layer followed by a 3-μm-thick InP (Si: 1.5×10^{16} cm^{-3}) cladding layer and a 200-nm-thick $In_{0.53}Ga_{0.47}As$ (Si: 1.5×10^{16} cm^{-3}) waveguide layer. Then, two 25-repetition stacks of active regions, the bottom one designed for the peak gain at 8.5 μm and the top one designed for the peak gain at 9.5 μm, were grown with $In_{0.53}Ga_{0.47}As/In_{0.52}Al_{0.48}As$ superlattices doped on average to 5.2×10^{16} cm^{-3}. The layer sequence of one period of the bottom active region, starting from the exit barrier, is **41**/18/7/55/**9**/53/**11**/48/**15**/37/**16**/35/**16**/33/**18**/31/**20**/29/**24**/27/**26**/27/**30**/27, and that of the top active region is **38**/20/**9**/60/**9**/59/**10**/50/**11**/40/**15**/34/**15**/33/**16**/30/**19**/30/**23**/31/**25**/32/**29**/30, where the layer thickness is in Angstrom, and the bold and underlined characters denote the $In_{0.52}Al_{0.48}As$ layers and doped (Si: 3.4×17 cm^{-3}) layers, respectively. The active regions were capped with a 300-nm-thick $In_{0.53}Ga_{0.47}As$ (Si: 1.5×10^{16} cm^{-3}) waveguide layer, a 3-μm-thick InP (Si: 1.5×10^{16} cm^{-3}) cladding layer, a 100-nm-thick InP (Si: 2.0×10^{18} cm^{-3}) contact layer, and finally a 10-nm-thick $In_{0.53}Ga_{0.47}As$ (Si: 1.0×10^{19} cm^{-3}) capping layer.

The laser gain of the processed Fabry–Perot devices was determined to peak around 9–10 μm, slightly shifted from the design position of 8.5–9.5 μm. A 15 mm by 20 mm section of the wafer was then processed into distributed feedback (DFB) lasers with the side current injection scheme [10] following conventional dry-etched ridge waveguide fabrication steps. The first-order surface gratings with two sections for selecting two mid-IR pump frequencies were formed using electron-beam lithography and dry etching. The grating pitches for the 9.02 μm short wavelength (λ_{short}) and the 10.08 μm long (λ_{long}) wavelength pumps are 1.408 and 1.584 μm, respectively. The completely processed wafer die was cleaved into two sections, one for the characterization of the reference devices on the InP substrate and the other for transfer to Si.

Figure 3 shows the transfer-printing process developed for our Si-hybrid DFG-QCL. The processed wafer was first coated with SU-8 epoxy resin (MicroChem Corp.) and 50-μm-wide 8-μm-tall supporting elements next to each ridge were defined lithographically in order to prevent epi-layer damage during the bonding process. The wafer was then attached to a glass slide with laser ridges facing the glass using crystal glue (Crystalbond 509). The InP substrate was then selectively removed using an HCl-based wet etchant with the InGaAs current injection layer used as an etch stop. The exposed surface of the current injection layer

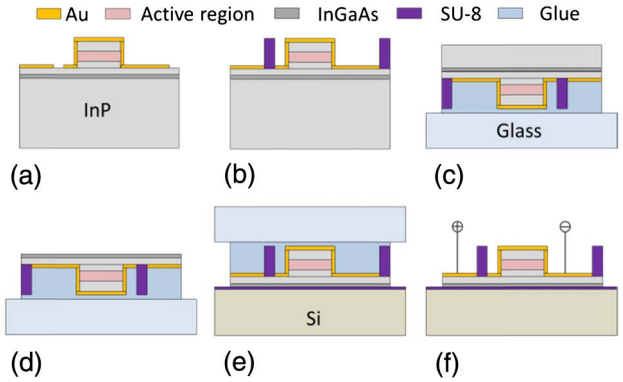

Fig. 3. Transfer-printing process. (a) Fully processed QCL on InP. (b) SU-8 supporting elements are formed. (c) Devices with the SU-8 supporting elements are bonded on a piece of a glass slide with crystal glue. (d) The InP substrate is removed. (e) The QCL is bonded to a Si substrate with SU-8 adhesive. (f) The glass slide and crystal glue are removed.

was then bonded to a 1-mm-thick FZ HR Si wafer coated with a 100-nm-thick SU-8 layer. The bonding was performed in the AML wafer bonding machine at a pressure of 1 MPa and a temperature of 180°C for 15 min. Under these conditions, the SU-8 layer was cured, leaving a strong permanent bond. Finally, the glass slide was removed by dissolving the crystal glue with acetone, and the hybrid QCL-on-Si wafer was diced into laser bars using a dicing saw. The front facets of the Si-hybrid and reference InP devices were polished in 15° and 30°, respectively, to outcouple THz Cherenkov emission in the direction parallel to the laser cavity.

We note that the transfer-printing of the QCL reported here allows for transferring completely processed devices, including buried hetero-structure lasers, to virtually any substrate. Our method is applicable to any QCLs and may, in particular, be used to produce III–V/Si hybrid QCLs for mid-IR photonic integrated circuits [20].

Figure 4 shows the cross-section scanning electron microscopy images of the devices on InP and Si substrates. No visible defects at the bonding interface are observed, and the transferred devices were

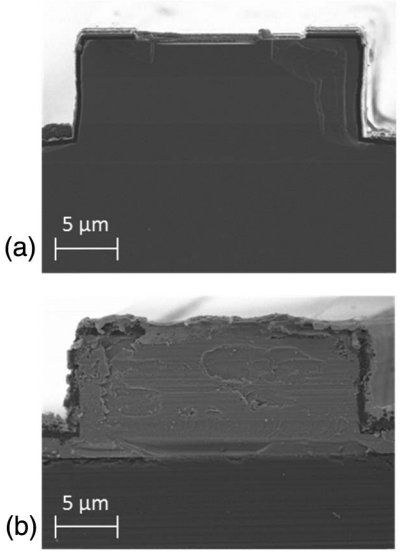

Fig. 4. Scanning electron microscope images of devices' facets. (a) The reference InP device. (b) The Si-hybrid device.

mechanically robust and operated with high yield, indicating good bonding quality. The somewhat roughened surface of the facet of the QCL-on-Si originates from the dicing process. The thickness of the SU-8 bonding layer is estimated to be 100 nm from the images in Fig. 4. According to our simulations, a 100-nm-thick SU-8 layer transmits about 90% of the Cherenkov THz DFG into the Si substrate, compared to the device without the adhesion layer simulated in Fig. 2(d). The refractive index of SU-8 ($n_{\text{SU-8}} = 1.7 + i \times 0.0355$) in the THz range is estimated from Ref. [25].

Devices were indium-soldered to copper blocks in the episide-up direction and wire bonded. The mid-IR power output was measured using a thermopile detector with a metal pipe, while the THz power output was measured using a two parabolic mirror setup and a liquid helium cooled Si bolometer. Both mid-IR and THz data were not corrected for collection efficiency. A long-pass filter with cut-on frequency of 1000 cm^{-1} was used to separate the two mid-IR pump powers. The spectra were measured using a Fourier transform infrared spectrometer equipped with a deuterated triglycine sulfate detector (for mid-IR measurements) or the Si bolometer (for THz measurements). Devices were driven in pulsed mode using 40 ns current pulses at 15 kHz repetition frequency at 20°C of a heat sink temperature.

4. CHARACTERIZATION

Figure 5 displays the mid-IR and THz spectra measured from the hybrid DFG-QCL-on-Si device. Stable dual single-mode operation with peak wavelengths of 994 and 1110 cm^{-1} is obtained. The peak positions of the mid-IR pumps are identical for devices on Si and InP. THz emission of both devices is at 3.48 THz, in agreement with the frequency separation of the mid-IR pumps.

Figure 6(a) shows the mid-IR power output for each pump. To compare the performance of the InP and Si devices, a best-performing device of each type with the identical dimensions (22 μm width and 4.2 mm cavity length) was selected for comparison. Both devices show nearly the same threshold current of 4.5 A for the short wavelength pump, while the long wavelength pump of the hybrid device starts lasing at 6.5 A. The threshold and power balance of the mid-IR pumps largely depends on the position of the cleaved laser facet relative to the DFB grating [26] and is difficult to control. Because of the gain competition

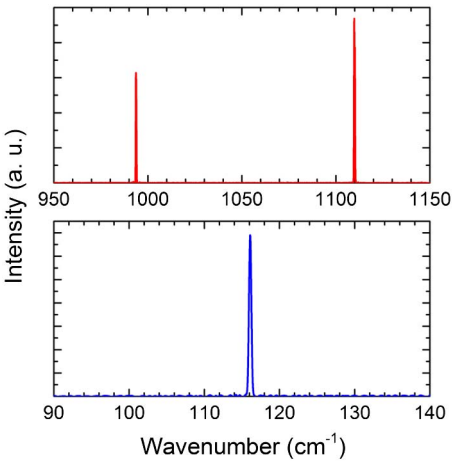

Fig. 5. Emission spectra. Mid-IR (top) and THz (bottom) spectra of the Si-hybrid device (22 μm width and 4.2 mm length) biased under pulsed current (15 kHz repetition rate and 40 ns pulse width) at 20°C.

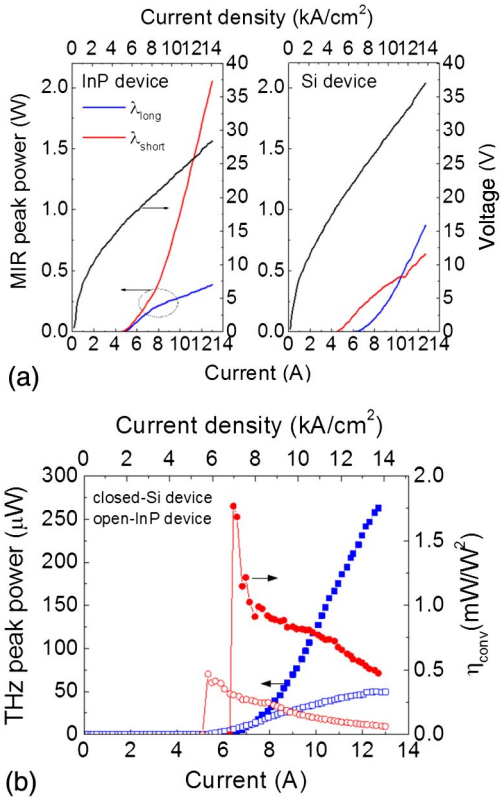

Fig. 6. Room-temperature device performance. (a) Mid-IR light-current-voltage characteristic of the InP device (left) and the Si device (right) operated in pulsed mode at 20°C. The blue, red, and black indicate the long wavelength pump (λ_{long}), the short wavelength pump (λ_{short}), and the device voltage, respectively. (b) THz power output (blue squares) and the mid-IR-to-THz conversion efficiency (red circles) of the InP device (open symbols) and the Si device (closed symbols).

between mid-IR modes, small differences in the feedback may result in a large difference in the threshold currents for the two mid-IR pumps [14,15,23]. Similarly strong variations in the threshold gain of the two mid-IR pumps were observed in devices on InP substrates (not shown in the paper). Overall, the performance of the Si-transferred devices was similar to that on InP for pulsed operation used in this work. For pulsed operation with higher duty cycles and continuous-wave operation, the Si-transferred devices will need to be operated in the episide-down configuration to avoid inefficient heat removal through the bonding interface.

The bias voltage of the Si device is about 5 V higher than that of the InP device, likely due to the reduced thickness of the current injection layer during substrate etching, which can be overcome in the future by using a thicker current injection layer.

THz peak power and the mid-IR-to-THz conversion efficiency of both devices are plotted together in Fig. 6(b) as functions of pump current. THz power of the device on the InP substrate is as high as 50 μW with conversion efficiency of 60 $\mu W/W^2$, while that of the device on the Si substrate reaches to 270 μW with efficiency of 480 $\mu W/W^2$ at the maximum bias current, resulting in a factor of 5 improvement in THz power and a factor of 8 improvement in the conversion efficiency. The power improvement is in excellent agreement with the simulation result, shown in Fig. 2(c). The ratio of the THz power of the hybrid

Table 1. THz DFG-QCL Device Performance at 10 A of Pump Current[a]

Device	$\eta_{\text{slope-THz}}$ (μW/A)	THz Power (μW)	η_{conv} (mW/W^2)
InP 1	6.9	35.2	0.13
InP 2	7.8	26.5	0.05
Si 1	54.3	123.3	0.79
Si 2	44.4	113.8	0.37
Si 3	47.1	146.9	0.58

[a]All devices were 22-μm-wide and 4.2-mm-long ridge-waveguide lasers with identical DFB grating design described in the text. The parameters $\eta_{\text{slope-THz}}$ and η_{conv} indicate the slope efficiency of the THz power output and the mid-IR-to-THz conversion efficiency, respectively.

device to that of the reference device remains nearly constant over the measured current range.

It should be noted that the intensity distribution of the mid-IR pumps in the laser cavity may vary significantly between samples, depending on the position of the cleaved laser facet relative to the DFB grating, as discussed in Ref. [27]. Therefore, the mid-IR-to-THz conversion efficiency (defined as the ratio of the THz power output to the product of the powers of the two mid-IR pumps emitted from the front facet of the laser [5,7]) may vary significantly from device to device. Table 1 lists the testing results of two devices on the InP substrate and three devices on the Si substrate. Their dimensions and the substrate polishing angles were identical to those described earlier. The results show that Si devices have consistently produced 3–6 times higher THz power output, compared to InP devices. The mid-IR-to-THz conversion efficiency of the tested Si devices was 3–16 times higher than that of the InP devices.

As discussed earlier, the Cherenkov wave in THz DFG-QCLs on Si can be outcoupled without facet polishing. Si devices with no facet polishing were tested in pulsed mode under the bias conditions described earlier. The power output was directed to the optical collection system by rotating the device by about 40° (see the inset of Fig. 7 for the simulated far-field emission of this device). The device performance was overall similar to that of the DFG-QCL with the polished Si substrate reported in Fig. 6.

Figure 8 shows the measured and calculated far-field profiles along the vertical direction of the Si and InP devices. The profiles were obtained by scanning the Si bolometer at a distance of 10 cm from the laser facet, as shown in the inset of Fig. 8(c). All devices show the far-field profile in the vertical direction close to a Gaussian shape with peak positions at 35° for the unpolished Si device, −2.5° for the polished Si device, and −6° for the InP device. The peak positions are in excellent agreement with simulations, assuming the mid-IR group index of 3.37. Further inspection shows that the full width at half-maximum (FWHM) values of the devices range from 9° to 17°.

The measured vertical far-field profiles of the THz emission are displayed together with the calculated profiles (shown in Fig. 8 in blue) based on the Fraunhofer approximation, $I(\theta) \propto \left| \int_{-W_a/2}^{W_a/2} U(x) e^{ik_{\text{THz}} \sin\theta x} dx \right|^2$, where k_{THz} is the THz wave vector in free space, W_a is the effective aperture width, and $U(x)$ is the distribution of the Cherenkov radiation field intensity along the transverse direction, x. [28] The values of W_a and $U(x)$ were determined by considering the cavity length of the device, the Cherenkov angle, the facet polishing angle, the substrate thickness, and the substrate loss. The FWHM values of the measured and simulated profiles are indicated in Fig. 8. The measured far field of the InP device shows excellent agreement with the simulated one, while those Si devices show 2.5 times larger beam

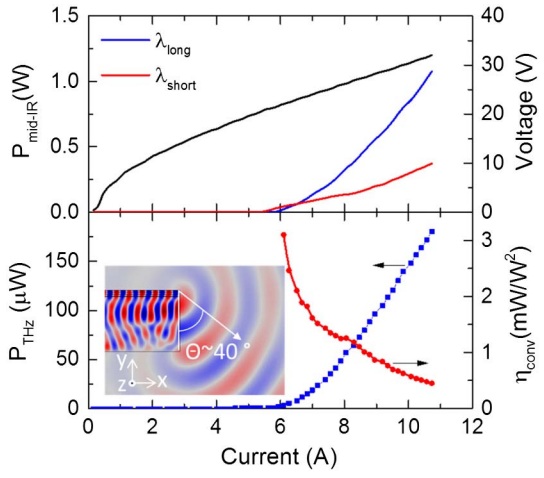

Fig. 7. Performance of the unpolished Si device. (Top) Mid-IR light-current-voltage characteristic of the 22 μm wide and 4.2 mm long device operated in pulsed mode at 20°C. The blue, red, and black indicate the long wavelength pump (λ_{long}), the short wavelength pump (λ_{short}), and the device voltage, respectively. (Bottom) THz power (blue squares) and the mid-IR-to-THz conversion efficiency (red circles) of the device under the same operating conditions. The inset displays the simulated magnetic field (H_z) of the THz output of the device. THz radiation is out-coupled from the facet at an angle of approximately 40°.

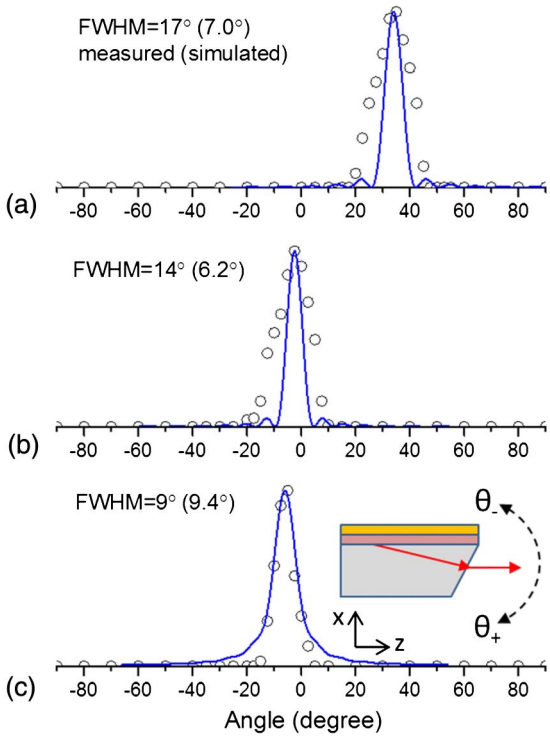

Fig. 8. Slow axis far fields of (a) the unpolished Si device, (b) the polished (15°) Si device and (c) the polished (30°) InP device. The open circles and solid lines indicate the measured and calculated results, respectively. The reference angle (0°) is defined as the beam direction parallel to the laser cavity. The polarity of the angle is described in the inset.

widths than the simulated one. The discrepancy between theory and experiment could be due to the imperfections in the device dicing and substrate polishing, small variation in the mid-IR group index along the laser cavity length due to ridge width roughness, and the non-uniform intensity distribution of the mid-IR pumps along the laser cavity, which affects the THz near-field profile at the substrate facet. The THz light scattering at the bonding interface might also be one of the reasons for the observed discrepancy. However, we did not observe any evidence of voids or non-uniformities in the bonding layer in our devices.

5. CONCLUSION

We have demonstrated that the use of FZ HR Si substrates instead of SI InP substrates in THz DFG-QCLs results in a dramatic improvement in THz power output and mid-IR-to-THz conversion efficiency in these devices. Experimentally, 22-μm-wide and 4.2-mm-long ridge-waveguide THz DFG-QCLs transfer-printed on FZ HR Si produced peak THz power output of 270 μW with mid-IR-to-THz conversion efficiency of 480 $\mu W/W^2$, while the reference InP device with the same dimensions produced 50 μW with conversion efficiency of 60 $\mu W/W^2$ at the maximum bias current. The transfer-printing method of QCLs onto foreign substrates described in this work is also expected to be useful for the creation of photonic integrated circuits of different functionalities in the mid-IR and THz spectral regions.

Funding. National Science Foundation (NSF) (ECCS-1150449, ECCS-1408511, IIP-1448707); Army Research Office (ARO) (W911NF-15-1-0630); Kwanjeong Educational Foundation (KEF) (12AmB06G).

REFERENCES

1. P. H. Siegel, "Terahertz technology," IEEE Trans. Microwave Theory Tech. **50**, 910–928 (2002).
2. M. Tonouchi, "Cutting-edge terahertz technology," Nat. Photonics **1**, 97–105 (2007).
3. S. Kumar, "Recent progress in terahertz quantum cascade lasers," IEEE J. Sel. Top. Quantum Electron. **17**, 38–47 (2011).
4. L. Li, L. Chen, J. Zhu, J. Freeman, P. Dean, A. Valavanis, A. G. Davies, and E. H. Linfield, "Terahertz quantum cascade lasers with >1 W output powers," Electron. Lett. **50**, 309–311 (2014).
5. M. A. Belkin, Q. J. Wang, C. Pflugl, A. Belyanin, S. P. Khanna, A. G. Davies, E. H. Linfield, and F. Capasso, "High-temperature operation of terahertz quantum cascade laser sources," IEEE J. Sel. Top. Quantum Electron. **15**, 952–967 (2009).
6. S. Fathololoumi, E. Dupont, C. W. I. Chan, Z. R. Wasilewski, S. R. Laframboise, D. Ban, A. Mátyás, C. Jirauschek, Q. Hu, and H. C. Liu, "Terahertz quantum cascade lasers operating up to ~200 K with optimized oscillator strength and improved injection tunneling," Opt. Express **20**, 3866—3876 (2012).
7. M. A. Belkin, F. Capasso, A. Belyanin, D. L. Sivco, A. Y. Cho, D. C. Oakley, C. J. Vineis, and G. W. Turner, "Terahertz quantum-cascade-laser source based on intracavity difference-frequency generation," Nat. Photonics **1**, 288–292 (2007).
8. M. A. Belkin and F. Capasso, "New frontiers in quantum cascade lasers: high performance room temperature terahertz sources," Phys. Scr. **90**, 118002 (2015).
9. M. A. Belkin, F. Capasso, F. Xie, A. Belyanin, M. Fischer, A. Wittmann, and J. Faist, "Room temperature terahertz quantum cascade laser source based on intracavity difference-frequency generation," Appl. Phys. Lett. **92**, 201101 (2008).
10. K. Vijayraghavan, R. W. Adams, A. Vizbaras, M. Jang, C. Grasse, G. Boehm, M. C. Amann, and M. A. Belkin, "Terahertz sources based on Čherenkov difference-frequency generation in quantum cascade lasers," Appl. Phys. Lett. **100**, 251104 (2012).
11. K. Vijayraghavan, Y. Jiang, M. Jang, A. Jiang, K. Choutagunta, A. Vizbaras, F. Demmerle, G. Boehm, M. C. Amann, and M. A. Belkin, "Broadly tunable terahertz generation in mid-infrared quantum cascade lasers," Nat. Commun. **4**, 2021 (2013).
12. S. Jung, A. Jiang, Y. Jiang, K. Vijayraghavan, X. Wang, M. Troccoli, and M. A. Belkin, "Broadly tunable monolithic room-temperature terahertz quantum cascade laser sources," Nat. Commun. **5**, 4267 (2014).
13. Q. Y. Lu, S. Slivken, N. Bandyopadhyay, Y. Bai, and M. Razeghi, "Widely tunable room temperature semiconductor terahertz source," Appl. Phys. Lett. **105**, 201102 (2014).
14. A. Jiang, S. Jung, Y. Jiang, K. Vijayraghavan, J. H. Kim, and M. A. Belkin, "Widely tunable terahertz source based on intra-cavity frequency mixing in quantum cascade laser arrays," Appl. Phys. Lett. **106**, 261107 (2015).
15. Y. Jiang, K. Vijayraghavan, S. Jung, F. Demmerle, G. Boehm, M. C. Amann, and M. A. Belkin, "External cavity terahertz quantum cascade laser sources based on intra-cavity frequency mixing with 1.2–5.9 THz tuning range," J. Opt. **16**, 094002 (2014).
16. M. Razeghi, Q. Y. Lu, N. Bandyopadhyay, W. Zhou, D. Heydari, Y. Bai, and S. Slivken, "Quantum cascade lasers: from tool to product," Opt. Express **23**, 8462–8475 (2015).
17. Q. Lu, D. Wu, S. Sengupta, S. Slivken, and M. Razeghi, "Room temperature continuous wave, monolithic tunable THz sources based on highly efficient mid-infrared quantum cascade lasers," Sci. Rep. **6**, 23595 (2016).
18. A. W. Fang, H. Park, O. Cohen, R. Jones, M. J. Paniccia, and J. E. Bowers, "Electrically pumped hybrid AlGaInAs-silicon evanescent laser," Opt. Express **14**, 9203–9210 (2006).
19. D. Liang and J. E. Bowers, "Recent progress in lasers on silicon," Nat. Photonics **4**, 511–517 (2010).
20. A. Spott, J. Peters, M. L. Davenport, E. J. Stanton, C. D. Merritt, W. W. Bewley, I. Vurgaftman, C. S. Kim, J. R. Meyer, J. Kirch, L. J. Mawst, D. Botez, and J. E. Bowers, "Quantum cascade laser on silicon," Optica **3**, 545–551 (2016).
21. H. Yang, D. Zhao, S. Chuwongin, J.-H. Seo, W. Yang, Y. Shuai, J. Berggren, M. Hammar, Z. Ma, and W. Zhou, "Transfer-printed stacked nanomembrane lasers on silicon," Nat. Photonics **6**, 615–620 (2012).
22. J. Justice, C. Bower, M. Meitl, M. B. Mooney, M. A. Gubbins, and B. Corbett, "Wafer-scale integration of group III-V lasers on silicon using transfer printing of epitaxial layers," Nat. Photonics **6**, 612–616 (2012).
23. Y. Jiang, K. Vijayraghavan, S. Jung, A. Jiang, J. H. Kim, F. Demmerle, G. Boehm, M. C. Amann, and M. A. Belkin, "Spectroscopic study of terahertz generation in mid-infrared quantum cascade lasers," Sci. Rep. **6**, 21169 (2016).
24. J. Faist, M. Beck, T. Aellen, and E. Gini, "Quantum-cascade lasers based on a bound-to-continuum transition," Appl. Phys. Lett. **78**, 147–149 (2001).
25. M. Naftaly and R. E. Miles, "Terahertz time-domain spectroscopy for material characterization," Proc. IEEE **95**, 1658–1665 (2007).
26. B. G. Lee, M. A. Belkin, R. Audet, J. MacArthur, L. Diehl, C. Pflügl, F. Capasso, D. C. Oakley, D. Chapman, A. Napoleone, D. Bour, S. Corzine, G. Höfler, and J. Faist, "Widely tunable single-mode quantum cascade laser source for mid-infrared spectroscopy," Appl. Phys. Lett. **91**, 231101 (2007).
27. B. G. Lee, M. A. Belkin, C. Pflügl, L. Diehl, H. A. Zhang, R. M. Audet, J. MacArthur, D. Bour, S. Corzine, G. Höfler, and F. Capasso, "Distributed feedback quantum cascade laser arrays," IEEE J. Quantum Electron. **45**, 554–565 (2009).
28. L. A. Coldren and S. W. Corzine, *Diode Lasers and Photonic Integrated Circuits* (Wiley, 1995).